

Hovering of an actively driven fluid-lubricated foil

Stéphane Poulain,¹ Timo Koch,¹ L. Mahadevan,^{2,3,*} and Andreas Carlson^{1,†}

¹*Department of Mathematics, University of Oslo, 0851 Oslo, Norway*

²*School of Engineering and Applied Sciences, Harvard University, Cambridge, Massachusetts 02138, USA*

³*Departments of Physics, and of Organismic and Evolutionary Biology, Harvard University, Cambridge, Massachusetts 02138, USA*

Inspired by recent experimental observations of a harmonically excited elastic foil hovering near a wall while supporting substantial weight, we develop a theoretical framework that describes the underlying physical effects. Using elasto-hydrodynamic lubrication theory, we quantify how the dynamic deformation of the soft foil couples to the viscous fluid flow in the intervening gap. Our analysis shows that the soft foil rectifies the reversible forcing, breaking time-reversal symmetry; the relative spatial support of the forcing determines whether the sheet is attracted to or repelled from the wall. A simple scaling law predicts the time-averaged equilibrium hovering height and the maximum weight the sheet can sustain before detaching from the surface. Numerical simulations of the governing equation corroborate our theoretical predictions, are in qualitative agreement with experiments, and might explain the behavior of organisms while providing design principles for soft robotics.

Hovering near surfaces has evolved in animals across diverse environments: insects hover above water and plants, birds hover above land and water, and fish hover in benthic environments and near other animals [1]. This phenomenon has also long inspired visionary science fiction writers and engineers alike, and hovering-based technology is now employed in various applications [2]. Although hovering flight is primarily associated with large-scale, high Reynolds number flows, it is not restricted to this regime. In viscous fluids, soft objects moving along a wall create lift forces through elasto-hydrodynamic coupling [3], a mechanism with a wide range of applications in biology, microfluidics, and nanoscience [4–9]. Also, hydrodynamic interactions coupled with unsteady elastic deformations of a foil enable its levitation above surfaces, even in the absence of inertia [10, 11].

Recent experiments reveal a striking manifestation of related ideas in contactless robotic manipulation, whereby an actively driven elastic foil lifts a heavy load while hovering just below a rigid surface, akin to a contactless suction cup [12]. Current explanations for this hovering are based on compressible and inertial effects in the surrounding fluid [13] but overlook the potentially crucial effects generated by elastic deformations of the foil. Here, we combine scaling estimates, asymptotic models, and numerical simulations of the governing equations to show that accounting for the underlying viscous elasto-hydrodynamics is critical in explaining the hovering of actively driven foils. We reveal how a periodic drive can lead to an aperiodic response, and predict the average height of hovering and the maximum load that can be sustained, consistent with experimental observations.

Setup. To describe hovering near a wall, we consider an elastic sheet of radius \tilde{L} subjected to a normal harmonic force of amplitude \tilde{F}_a and angular frequency $\tilde{\omega}$. The associated load $\tilde{\sigma}_a \cos(\tilde{\omega}\tilde{t})$ is uniformly distributed over a disk of radius $\tilde{\ell}$, see Fig. 1. The sheet has a den-

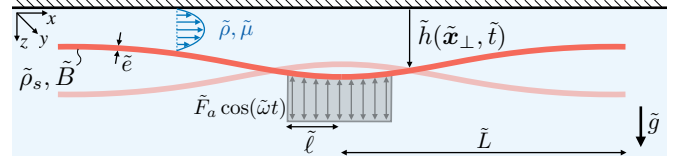


FIG. 1. Schematic of an elastic sheet of bending rigidity \tilde{B} , radius \tilde{L} , thickness \tilde{e} and density $\tilde{\rho}_s$ immersed in a fluid of density $\tilde{\rho}$ and viscosity $\tilde{\mu}$ in the presence of gravity \tilde{g} . The sheet bends in response to a harmonic normal force $\tilde{F}_a \cos(\tilde{\omega}\tilde{t})$, distributed over an area of radius $\tilde{\ell}$, which drives a flow in the thin gap.

sity $\tilde{\rho}_s$, Young's modulus \tilde{E} , Poisson's ratio ν , and thickness \tilde{e} ; its bending modulus is $\tilde{B} = \tilde{E}\tilde{e}^3/12(1-\nu^2)$. The gravitational acceleration \tilde{g} is normal to the wall. The surrounding incompressible fluid has a dynamic viscosity $\tilde{\mu}$ and density $\tilde{\rho}$. The characteristic film height separating the sheet and the wall is \tilde{H} . Experiments [12] have been performed in air ($\tilde{\mu} \simeq 2 \times 10^{-5}$ Pa s, $\tilde{\rho} \simeq 1.2$ kg m⁻³) using thin sheets ($\tilde{e} \simeq 200$ μ m, $\tilde{L} \simeq 4.5$ cm) made of plastic ($\tilde{E} \simeq 3$ GPa, $\nu \simeq 0.3$, $\tilde{\rho}_s \simeq 1400$ kg m⁻³). An eccentric mass motor ($\tilde{\ell} \simeq 1$ cm), i.e., a mass $\tilde{m} \simeq 0.6$ g rotating with $\tilde{\omega} \simeq 1300$ s⁻¹ and with a gyration radius $\tilde{r} \simeq 1$ mm, provides a force $\tilde{F}_a = \tilde{m}\tilde{r}\tilde{\omega}^2 \simeq 1$ N.

Scaling predictions. When the foil is actively driven, the viscous stresses in the thin fluid gap (Fig. 1) scale as $\tilde{\mu}\tilde{\omega}\tilde{L}^2/\tilde{H}^2$ and the sheet's bending stresses as $\tilde{B}\tilde{H}/\tilde{L}^4$. At equilibrium, the stresses balance, giving a characteristic height scale $\tilde{H}_{bv} \sim \tilde{L}^2(\tilde{\mu}\tilde{\omega}/\tilde{B})^{1/3} = \mathcal{O}(1$ mm). Using the parameter values above, these stresses are $\mathcal{O}(1$ Pa), while the active stress $\tilde{\sigma}_a \sim \tilde{F}_a/\tilde{\ell}^2 = \mathcal{O}(10^3$ Pa), suggesting that the sheet deforms significantly. In fact, the weight \tilde{W} the sheet can bear should depend on both the active force and the sheet's softness since a rigid sheet is incapable of supporting any weight. We expected \tilde{W} to increase as the bending force \tilde{F}_b decreases, with $\tilde{F}_b \sim (\tilde{\mu}\tilde{\omega}\tilde{B}^2)^{1/3}$

when evaluated at \tilde{H}_{bv} . Moreover, \tilde{W} may only depend on even powers of the active force amplitude: reversing the sign of \tilde{F}_a is equivalent to a phase shift, which cannot affect the long-term dynamics. We therefore predict, on dimensional grounds, $\tilde{W} \sim \tilde{F}_a^2/\tilde{F}_b = \tilde{F}_a^2/(\tilde{\mu}\tilde{\omega}\tilde{B}^2)^{1/3}$. In what follows, we verify these simple scaling arguments and demonstrate, using asymptotic analysis and numerical simulations, how active soft sheets are attracted to or repelled from surfaces.

Governing equations. We assume that the fluid-filled gap between the sheet and the wall is narrow, $\tilde{H}/\tilde{L} \ll 1$, and that the Reynolds number is small, $\text{Re} = \tilde{\rho}\tilde{\omega}\tilde{H}^2/\tilde{\mu} \ll 1$ so that inertial effects are negligible. Consequently, we use lubrication theory [14] to describe the flow. Balancing the horizontal pressure gradient with the transverse viscous stresses yields an evolution equation for $\tilde{h}(\tilde{\mathbf{x}}_\perp, \tilde{t})$, the distance between the sheet and the wall at the horizontal position $\tilde{\mathbf{x}}_\perp = (\tilde{x}, \tilde{y})$ (Fig. 1):

$$12\frac{\partial h}{\partial t} - \nabla_\perp \cdot (h^3 \nabla_\perp p) = 0, \quad (1)$$

with $\mathbf{q} = -h^3 \nabla_\perp p$ the horizontal volumetric flux. The governing equations and results are presented in dimensionless units (written without tilde throughout the Letter), with $\mathbf{x}_\perp = \tilde{\mathbf{x}}_\perp/\tilde{L}$, $\ell = \tilde{\ell}/\tilde{L}$, $t = \tilde{t}\tilde{\omega}$, $h = \tilde{h}/\tilde{H}$, $p = \tilde{p}\tilde{H}^2/\tilde{\mu}\tilde{\omega}\tilde{L}^2$. The gage pressure \tilde{p} is measured relative to the atmospheric pressure, and $\nabla_\perp = (\partial/\partial x, \partial/\partial y)$ is the horizontal gradient. We keep the height scale \tilde{H} arbitrary unless otherwise specified. By assuming an elastic sheet with small deformations (such that it bends without stretching) and no inertial effects, the normal stress balance follows Kirchhoff-Love theory [15, 16]:

$$\begin{aligned} -p &= \nabla_\perp \cdot (\nabla_\perp \cdot \mathbf{M}) + f_a(\mathbf{x}_\perp, t) + \mathcal{G}, \\ \mathbf{M} &= -\mathcal{B}[(1-\nu)\boldsymbol{\kappa} - \nu \text{tr}(\boldsymbol{\kappa})], \end{aligned} \quad (2)$$

with $\mathcal{B} = \tilde{B}\tilde{H}^3/\tilde{\mu}\tilde{\omega}\tilde{L}^6$ the ratio between bending and viscous stresses, $\mathcal{G} = (\tilde{\rho}_s - \tilde{\rho})\tilde{e}\tilde{g}\tilde{H}^2/\tilde{\mu}\tilde{\omega}\tilde{L}^2$ the ratio between areal weight and viscous stresses, \mathbf{M} the matrix of bending moments and $\boldsymbol{\kappa}$ the Hessian of h , the sheet's local curvature. The active normal stress f_a is distributed uniformly around the center of the sheet (Fig. 1): $f_a(\mathbf{x}_\perp, t) = \Gamma \cos(t)$ if $|\mathbf{x}_\perp| < \ell$, $= 0$ otherwise, with $\Gamma = \tilde{\sigma}_a\tilde{H}^2/\tilde{\mu}\tilde{\omega}\tilde{L}^2$ the ratio between active and viscous stresses. We expect qualitatively the same behavior for a one-dimensional (1D) and two-dimensional (2D) system and focus, for simplicity, the subsequent analyses on a 1D sheet: $\mathbf{x}_\perp \rightarrow x$, $\nabla_\perp \rightarrow \partial/\partial x$, $\partial/\partial y = 0$. As boundary conditions, we use the fact that the sheet's edges are stress-free, torque-free, and at atmospheric pressure: $p = \partial^2 h/\partial x^2 = \partial^3 h/\partial x^3 = 0$ for $x = \pm 1$.

Weightless sheet. First, we consider a weightless foil ($\mathcal{W} = 0$), which allows us to study the effect of the sheet's softness in isolation. We characterize the magnitude of the sheet's deformation with $\gamma = \Gamma\ell/\mathcal{B}$, the ratio of active and bending forces. In the limit $\gamma \rightarrow 0$, the sheet is

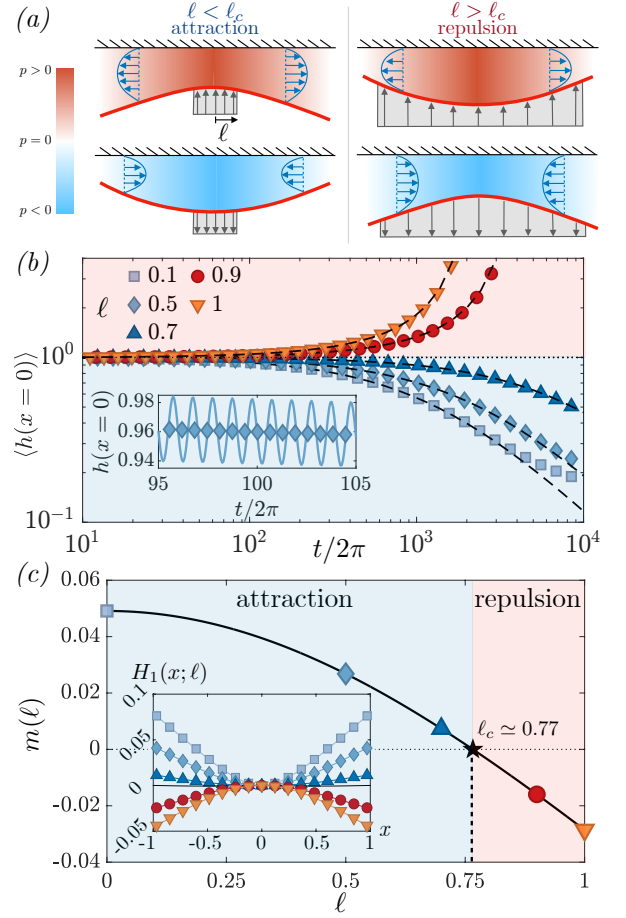


FIG. 2. (a) Schematic illustration of the load distribution and deformation of the sheet based on the value of ℓ . Supplementary Movies S1 and S2 provide additional visualizations [17]. (b) Numerical solutions of (1) and (2) for the time-evolution of the averaged height (symbols) for $\gamma = 0.1$, $\mathcal{G} = 0$. Dashed lines are the asymptotic result (4). The inset shows a time-resolved zoom for $\ell = 0.5$ that highlights the slow average compared to the fast oscillations (solid line). (c) The function $m(\ell)$ appears in (4) and determines whether the soft sheet is attracted ($m(\ell) > 0$) or repelled ($m(\ell) < 0$) from the wall. The shape of the sheet at $\mathcal{O}(\gamma)$ is $H_1(x; \ell) \cos(t)$, characterized in the inset.

flat and rigid, and the film height is only a function of time: (1) and (2) yield $p(x, t) = 3\Gamma\ell \cos(t) (1 - x^2)/2$ and $h(t) = (1 + \Gamma\ell \sin(t)/2)^{-1/2}$. The time-averaged height $\langle h \rangle(t) = \int_t^{t+2\pi} h(t) dt/2\pi$ is constant and the system dynamics is time-reversible. To predict the behavior when the sheet deforms, $\gamma > 0$, we integrate (1) over the length of the sheet and average in time to find $12(\partial h/\partial t) = -\langle q_e \rangle$, with $\langle q_e \rangle = -\langle h^3 \partial p/\partial x \rangle_{x=1}$ the time-averaged flux at the edge of the sheet. We expect that the sheet's elastic response at leading order is in phase with the forcing: $h(x, t) \simeq h_0(t) + \gamma \cos(t) H_1(x; \ell)$, with H_1 a function describing the sheet's deformation, which depends on the relative extent ℓ of the forcing. By using the pressure distribution obtained for the rigid

sheet, we find at leading order

$$\frac{\partial \langle h_0 \rangle}{\partial t} \sim - \frac{\langle h_0 \rangle^2 (\Gamma \ell)^2}{\mathcal{B}} H_1(1; \ell). \quad (3)$$

The deformation at the edge $H_1(1; \ell)$ is determined by the shape the sheet takes when it is subjected on one side to the parabolic fluid pressure across its entire length and on the other side to the active rectangular forcing of length 2ℓ (Fig. 2a). As $\ell \rightarrow 0$, the sheet's edges are only influenced by the fluid pressure and bend accordingly: $H_1(1; \ell) > 0$. Conversely, as $\ell \rightarrow 1$, the active forcing dominates the edges, and the sheet bends in the opposite direction. This indicates a critical length ℓ_c at which $H_1(1; \ell)$ changes sign, with the sheet being attracted to the wall for $\ell < \ell_c$ ($\partial \langle h_0 \rangle / \partial t < 0$) and repelled otherwise. A naïve estimate suggests that the shift occurs when the fluid pressure at the center of the sheet, $p(0, t) = 3\Gamma\ell \cos(t)/2$, and the active stress, $f_a(0, t) = \Gamma \cos(t)$, are similar, i.e. $\ell \simeq 2/3$; a more careful calculation below confirms that this is a reasonable estimate.

To verify go beyond these scaling predictions, we solve (1) and (2) numerically [17, 18]. Figure 2(a) and the supplementary movies S1-S3 [17] illustrate the coupling between the sheet's deformation and pressure distribution that leads to attraction or repulsion. Figure 2(b) shows that the sheet's averaged motion, characterized by $\langle h(0, t) \rangle$, is slow compared to the periodic forcing.

This observation motivates a two-timescale asymptotic expansion of the governing equations. We assume that the dynamics depend both on the time t associated with the active forcing and a slow time $\tau = \gamma t$ describing the averaged evolution: $h(x, t)$ becomes $h(x, t, \tau)$. We then expand h in powers of γ and the time derivative $\partial/\partial t$ as $\partial/\partial t \rightarrow \partial/\partial t + \gamma \partial/\partial \tau$. At $\mathcal{O}(\gamma^2)$, we find [17]:

$$\begin{aligned} h(x, t, \tau) &= h_0(t, \tau) + \gamma \cos(t) H_1(x; \ell) + \gamma h'_1(t, \tau) \\ &+ \gamma^2 \left[\frac{\sin(t)}{\Gamma \ell h_0^3(t, \tau)} H_2(x; \ell) + \frac{\cos^2(t)}{h_0(t, \tau)} H_2^*(x; \ell) \right], \quad (4) \\ h_0(t, \tau) &= \left[\left(1 + \frac{m(\ell)}{2} \Gamma \ell \tau \right)^2 + \frac{\Gamma \ell}{2} \sin(t) \right]^{-1/2}. \end{aligned}$$

The analytical expression of $m(\ell)$, $H_1(x; \ell)$, $H_2(x; \ell)$ and $H_2^*(x; \ell)$ are given in [17]. The function h'_1 has zero mean to $\mathcal{O}(\gamma)$ and does not contribute to the time-averaged evolution: $\langle h \rangle(0, t) \simeq (1 + 0.5(\Gamma \ell)^2 m(\ell) t / \mathcal{B})^{-1}$. This agrees with our predicted scaling (3) and with the numerical simulations, as shown in Fig. 2(b). The nature of the sheet's motion with respect to the wall is controlled by $m(\ell)$, which is directly correlated with $H_1(1, \ell)$, the sheet's deformation profile at leading order (Fig. 2c). In particular, we find $H_1(1; \ell) = (\ell^3 - 4\ell^2 + 1.9)/24$, corresponding to a critical motor size $\ell_c \simeq 0.77$ with the foil attracted to the wall for $\ell < \ell_c$ and repelled for $\ell > \ell_c$.

Curiously, attraction or repulsion takes place even though the forces acting on the sheet cancel on average: Eq. (2) gives $\langle p \rangle = \langle f_a \rangle = 0$. In fact, it is the deformations at $\mathcal{O}(\gamma^2)$ in (4) that break the time-reversible symmetry. Then the effective friction coefficients associated with moving toward and away from the wall are not equal, which works, similar to a ratchet, to enable net average motion.

Heavy sheet. For a heavy sheet ($\mathcal{G} \neq 0$) the elasto-hydrodynamic attraction/repulsion mechanism can balance the weight depending on the sign of $(\ell - \ell_c)$, and as discussed previously, an equilibrium height \tilde{H}_{bv} can arise when viscous and bending forces balance. Choosing $\tilde{H} = \tilde{H}_{bv}$ to nondimensionalize our system, we let $\alpha = \tilde{F}_a / \tilde{F}_b$ the ratio between the active and bending forces and rescale the weight by introducing $\mathcal{W} = \mathcal{G} / \alpha^2 = \tilde{W} \tilde{F}_b / \tilde{F}_a^2$. While a direct asymptotic analysis of this modified problem is challenging, to study hovering equilibria, we focus on the limit of an active point force, $\ell \rightarrow 0$, and use a Galerkin projection.

We consider N spatial modes and seek the height as $h(x, t) = h_0(t) + \alpha \cos(t) H_{1,0}(x) + \alpha^2 \mathcal{W} H_{1,1}(x) + \sum_{i=1}^N c_i(t) \zeta_i(x)$, with $h_0(t)$ and $(c_i(t))_{i=1 \dots N}$ unknown functions to be determined. The functions $H_{1,0}(x)$ and $H_{1,1}(x)$ are the polynomials obtained from the analysis leading to (4), cf. Fig. 2(c), and describe the first-order deformations due to an active point force and to a uniform weight, respectively. The functions ζ_i are the even eigenmodes of the triharmonic operator $\partial^6/\partial x^6$ subject to $\partial^2 \zeta / \partial x^2 = \partial^3 \zeta / \partial x^3 = \partial^4 \zeta / \partial x^4 = 0$ at $x = \pm 1$, which appears when linearizing (1) and (2) for small deformations (see [17] for details and Fig. A1 for a visualization). Using this ansatz, we project (1) and (2) in space and perform a two-timescale asymptotic expansion with the slow timescale $T = \alpha^2 t$ so that $h_0(t)$ becomes $h_0(t, T)$. After some algebra [17], this leads to a single differential equation governing the time-averaged height $\langle h_0 \rangle(T) = \int_t^{t+2\pi} h_0(t, T) dt / 2\pi$ at $\mathcal{O}(\alpha^2)$:

$$\begin{aligned} \frac{1}{\langle h_0 \rangle^2} \frac{d \langle h_0 \rangle}{dT} &= \frac{1}{4} \mathcal{W} \langle h_0 \rangle - d_0 + \sum_{i,j=1}^N d_{ij} g_{ij}(\langle h_0 \rangle), \quad (5) \\ g_{ij}(h) &= \frac{1 + (h/\sqrt{e_i e_j})^6}{(1 + (h/e_i)^6)(1 + (h/e_j)^6)}. \end{aligned}$$

The numerical coefficients e_i , d_{ij} and d_0 are given in [17]. The first term on the r.h.s. of (5) is the effect of gravity; the second term is the 1st-order effect of softness already found for the weightless sheet, cf. (3). The sum describes the effect of the excitation modes ζ_i , with $i = j$ corresponding to i -th mode and $i \neq j$ to the interaction between modes i and j . The coefficients d_{ij} describe the strength of the effect, and e_i corresponds to the height scale below which the i -th mode is excited: $g_{ij}(\langle h_0 \rangle) \simeq 0$ for $\langle h_0 \rangle \gg e_i$, $\langle h_0 \rangle \gg e_j$.

Equation (5) admits both stable and unstable steady

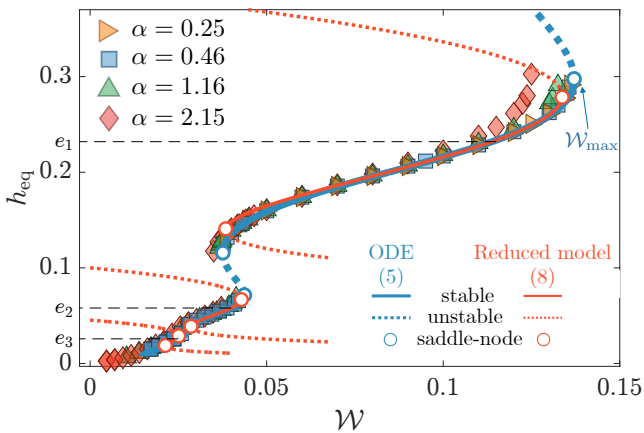


FIG. 3. Comparison between the bifurcation diagram obtained by numerical continuation of (5) (blue lines) with numerical results obtained from solving (1) and (2) with $\ell = 0.05$ for different α (symbols). The orange lines are obtained analytically from (8) and are derived in Appendix A; they correspond to the equilibria obtained by neglecting pairwise interactions between modes and assuming that the i -th vibration mode is only excited when $h_{\text{eq}} \ll e_i$, with $e_1 \simeq 0.23$, $e_2 \simeq 0.06$, $e_3 \simeq 0.03$. Each mode creates an equilibrium branch near $h_{\text{eq}} \simeq e_i$ through saddle-node bifurcations. In the actual system (5), the branches for $i \geq 2$ merge, and the system only exhibits two branches: one created by the first excitation mode and a second branch where all the modes are progressively excited as $\mathcal{W} \rightarrow 0$.

states as the weight \mathcal{W} is varied. Using numerical continuation [19] (truncating the sum after $N = 5$), we obtain the associated bifurcation diagram showing the steady state hovering height h_{eq} as a function of \mathcal{W} . We also numerically integrated the original partial differential equations (1) and (2) in 1D up until the averaged height reaches a steady state or diverges. Figure 3 shows that both approaches closely agree in predicting the stable equilibria, validating the asymptotic analysis leading to (5).

In either case, when $\mathcal{W} > \mathcal{W}_{\text{max}} \simeq 0.137$, the sheet cannot reach an equilibrium, and detaches from the wall with $\langle h_0 \rangle \rightarrow \infty$. As \mathcal{W} decreases, a stable equilibrium is created through a saddle-node bifurcation at $\mathcal{W} = \mathcal{W}_{\text{max}}$. As \mathcal{W} further decreases, the equilibrium height continuously decreases until the equilibrium is broken through another saddle-node bifurcation at $\mathcal{W} \simeq 0.038$. However, a second branch of stable equilibrium, corresponding to a lower height is created through a third saddle-node bifurcation at $\mathcal{W} \simeq 0.043$ and extends down to $\mathcal{W} \rightarrow 0$. There is a small hysteresis region between the two equilibrium branches such that an equilibrium height can be reached for all weights $0 < \mathcal{W} < \mathcal{W}_{\text{max}}$. Appendix A details an analytical study of (5). In short, as the weight decreases and the sheet gets closer to the substrate, higher-order modes are excited and create equilibria near $\langle h_0 \rangle \simeq e_i$. The first branch of the equilibrium curve shown in Fig. 3,

for $h_{\text{eq}} > 0.1$, corresponds to the excitation of the first mode ζ_1 , while the second branch includes progressively higher-order modes as $\mathcal{W} \rightarrow 0$, $h_{\text{eq}} \rightarrow 0$. The excitation of higher-order modes allows the sheet to store significant bending energy while keeping deformation amplitudes small when it approaches the wall, preventing contact. The supplementary movies S3-S5 [17] illustrate the dynamics predicted numerically and further highlight that higher-order modes are prominent for small hovering heights.

Discussion and conclusions. Extending our results to circular, axisymmetric sheets leads to qualitatively similar conclusions. The only differences are the numerical coefficients e_i , d_{ij} and d_0 appearing in (5), leading to a bifurcation diagram similar to that in Fig. 3 but with different values for \mathcal{W}_{max} and the equilibrium heights (see [17] for details). For a circular sheet with a Poisson's ratio $\nu = 0.3$, the maximum weight \tilde{W}_{max} the sheet can support and the hovering height \tilde{h}_{eq} are, in dimensional units:

$$\tilde{W}_{\text{max}} = 0.11 \frac{(\tilde{m}\tilde{r}\tilde{\omega}^2)^2}{(\tilde{\mu}\tilde{\omega}\tilde{B}^2)^{1/3}}, \quad (6)$$

$$\tilde{h}_{\text{eq}}(\tilde{W}_{\text{max}}) = 0.19 \left(\frac{\tilde{\mu}\tilde{\omega}}{\tilde{B}}\right)^{1/3} \tilde{L}^2.$$

These results are consistent with the scaling results for equilibrium height and load derived on page 1 using simple arguments. Although Equations (5) and (6) are based on the assumption of a point load, $\ell \rightarrow 0$, the scaling is qualitatively the same for a finite ($\ell > 0$) and stiff ($\mathcal{B} \rightarrow \infty$ for $|\mathbf{x}_{\perp}| < \ell$) motor, where the difference only enters in the prefactor (see Appendix B for details). Comparing our asymptotic results with the experiments of [12] using the parameter values described earlier, we find $\tilde{W}_{\text{max}} \simeq 9\text{N}$ and $\tilde{h}_{\text{eq}} \simeq 0.6\text{mm}$, reasonably close to the reported values $\tilde{W}_{\text{max}} \simeq 5\text{N}$ and $\tilde{h}_{\text{eq}} \simeq 0.8\text{mm}$.

Our analysis of the dynamic interplay between active forcing, viscous fluid flow, and bending stresses demonstrates how a soft foil is attracted to or repelled from a solid surface, depending on the spatial distribution of the forcing. This mechanism allows the foil to hover while sustaining a substantial weight, akin to a contactless suction cup. We anticipate that this hovering principle generalizes to a variety of forcing modalities, including active torques, and applies to a wide range of foil sizes and weight-bearing capacities in both air and water, with potential relevance for adhesive behavior in marine organisms [20]. More generally, our findings provide new physical insights into active elastohydrodynamic phenomena and open new avenues for the design of contactless grippers, soft robots, and related technological applications.

Acknowledgements. We thank Sami Al-Izzi, Annette Cazaubiel and Jingbang Liu for insightful discussions.

S.P and A.C acknowledge funding from the Research Council of Norway through project 341989. T.K. acknowledges funding from the European Union’s Horizon 2020 research and innovation programme under the Marie Skłodowska-Curie grant agreement No 801133. L.M. acknowledges funding from the Simons Foundation and the Henri Seydoux Fund.

* lmahadev@g.harvard.edu

† acarlson@math.uio.no

- [1] S. Vogel, *Life in moving fluids: the physical biology of flow* (Princeton university press, 1981).
- [2] E. Brandt, Levitation in Physics, *Science* **243**, 349 (1989).
- [3] J. Skotheim and L. Mahadevan, Soft lubrication, *Phys. Rev. Lett.* **92**, 245509 (2004).
- [4] S. Leroy, A. Steinberger, C. Cottin-Bizonne, F. Restagno, L. Léger, and E. Charlaix, Hydrodynamic interaction between a spherical particle and an elastic surface: A gentle probe for soft thin films, *Phys. Rev. Lett.* **108**, 264501 (2012).
- [5] B. Saintyves, T. Jules, T. Salez, and L. Mahadevan, Self-sustained lift and low friction via soft lubrication, *Proc. Natl. Acad. Sci* **113**, 5847 (2016).
- [6] M. Essink, A. Pandey, S. Karpitschka, C. Venner, and J. Snoeijer, Regimes of soft lubrication, *J. Fluid Mech.* **915**, A49 (2021).
- [7] N. Fares, M. Lavaud, Z. Zhang, A. Jha, Y. Amarouchene, and T. Salez, Observation of brownian elasto-hydrodynamic forces acting on confined soft colloids, *Proc. Natl. Acad. Sci.* **121**, e2411956121 (2024).
- [8] L. Bureau, G. Coupier, and T. Salez, Lift at low Reynolds number, *Eur. Phys. J. E* **46**, 111 (2023).
- [9] B. Rallabandi, Fluid-elastic interactions near contact at low Reynolds number, *Annu. Rev. Fluid Mech.* **56**, 491 (2024).
- [10] M. Argentina, J. Skotheim, and L. Mahadevan, Settling and swimming of flexible fluid-lubricated foils, *Phys. Rev. Lett.* **99**, 224503 (2007).
- [11] N. Jafferis, H. Stone, and J. Sturm, Traveling wave-induced aerodynamic propulsive forces using piezoelectrically deformed substrates, *Appl. Phys. Lett.* **99** (2011).
- [12] W. Weston-Dawkes, I. Adibnazari, Y.-W. Hu, M. Everman, N. Gravish, and M. Tolley, Gas-lubricated vibration-based adhesion for robotics, *Adv. Intell. Syst.* **3**, 2100001 (2021).
- [13] S. Ramanarayanan, W. Coenen, and A. Sánchez, Viscoacoustic squeeze-film force on a rigid disk undergoing small axial oscillations, *J. Fluid Mech.* **933** (2022).
- [14] G. Batchelor, *An Introduction to Fluid Dynamics* (Cambridge University Press, 1967).
- [15] S. Timoshenko and S. Woinowsky-Krieger, *Theory of plates and shells*, 2nd ed. (McGraw-hill New York, 1959).
- [16] L. Landau and E. Lifshitz, *Course of Theoretical Physics vol. 7: Theory of Elasticity* (3rd edn. Pergamon, 1986).
- [17] (2024), see Supplemental Material at URL-will-be-inserted-by-publisher for derivations.
- [18] T. Koch, D. Gläser, K. Weishaupt, *et al.*, DuMux 3 – an open-source simulator for solving flow and transport problems in porous media with a focus on model coupling, *Computers & Mathematics with Applications* **81**, 423 (2021).
- [19] A. Dhooge, W. Govaerts, and Y. Kuznetsov, MATCONT: a MATLAB package for numerical bifurcation analysis of ODEs, *ACM Trans. Math. Softw.* **29**, 141 (2003).
- [20] T. S. Chan and A. Carlson, Physics of adhesive organs in animals, *The European Physical Journal Special Topics* **227**, 2501 (2019).
- [21] D. Avitabile, D. Lloyd, J. Burke, E. Knobloch, and B. Sandstede, To snake or not to snake in the planar Swift–Hohenberg equation, *SIAM J. Appl. Dyn.* **9**, 704 (2010).

Appendix A: Analysis of Eq. (5) – The first three modes $\zeta_i(x)$ are shown in Fig. 3. Their analytical expressions are given in the Supplementary Materials [17].

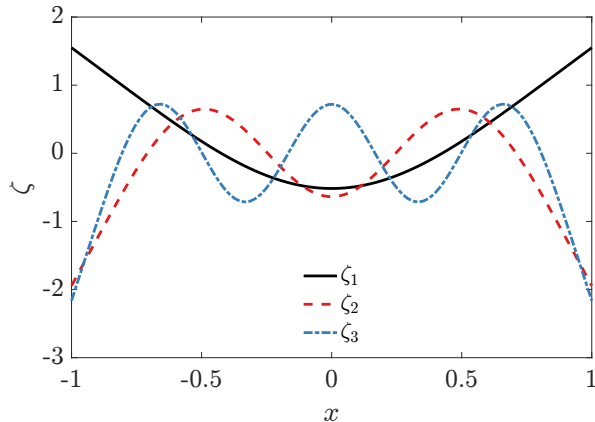


FIG. A1. First three modes $\zeta_i(x)$ in the Galerkin projection.

Equation (5) without considering the modes ζ_i (i.e. $N = 0$) reads

$$\frac{1}{\langle h_0 \rangle^2} \frac{d\langle h_0 \rangle}{dT} = \frac{1}{4} \mathcal{W} \langle h_0 \rangle - d_0. \quad (7)$$

A linear stability analysis shows that the only fixed point $4d_0/\mathcal{W}$ is unconditionally unstable.

To analyze (5) with the contribution of the modes ζ_i analytically, we neglect pairwise interactions ($d_{ij} = 0$ for $i \neq j$) and assume a scale separation $e_1 \gg e_2 \gg \dots$. We note that $g_{nn}(\langle h_0 \rangle) = 0$ if $\langle h_0 \rangle \gg e_n$, $g_{nn}(\langle h_0 \rangle) = 1$ if $\langle h_0 \rangle \ll e_n$. Thus, if $\langle h_0 \rangle$ is far from any of the heights e_n , the structure of (5) is the same as that of (7), and there is no stable equilibrium. To study the behavior near e_n , we write $\langle h_0 \rangle(t) = e_n (1 + \epsilon_n(t))$, insert in (5), and expand to 3rd order in $\epsilon_n(t)$. We then find that the fixed points of the dynamical system are solutions of the cubic equation:

$$A_n \epsilon_n^3 + B_n \epsilon_n^2 + C_n \epsilon_n + D_n = 0 \quad (8)$$

with coefficients

$$A_n = 4d_{nn}, \quad B_n = \frac{3}{4}d_{nn}, \quad C_n = \frac{\mathcal{W}}{4} - \frac{3d_{nn}}{2},$$

$$D_n = \frac{\mathcal{W}}{4} + \frac{d_{nn}}{2} - d_0 + \sum_{i=1}^{n-1} d_{ii}.$$

The number of solutions of (8) depends on the sign of the discriminant $\Delta_n = 18A_n B_n C_n D_n - 4B_n^3 D_n + B_n^2 C_n^2 - 4A_n C_n^3 - 27A_n^2 D_n^2$: either one solution for $\Delta_n > 0$, corresponding to one unstable equilibrium; or three solutions for $\Delta_n < 0$, corresponding to two unstable equilibria and one stable equilibrium. The transition between these two behaviors corresponds to saddle-node bifurcations.

The bifurcation diagrams predicted from these asymptotic expansions around e_n are shown in Fig. 3 for $n = 1, 2, 3$, where we note a close agreement with the complete bifurcation diagram of (4) obtained numerically. We observe a cascade of creation and destruction of equilibria as high-order modes get progressively excited for lighter sheets and smaller heights. We note that this is not unlike the snaking bifurcation diagram observed in the Swift-Hohenberg equation [21], but here arises in a very different setting. The main discrepancy is that the complete equilibrium diagram only shows two branches. The lower branches, corresponding to $n \geq 2$, are, in fact, all connected. This is because the assumption of scale separation is inaccurate for $n \geq 2$ (for example, $e_3/e_2 \simeq 0.44$, $e_4/e_3 \simeq 0.56$). However, the physical picture of higher-order mode excitations as $\mathcal{W} \rightarrow 0$, $h_{\text{eq}} \rightarrow 0$ remains accurate.

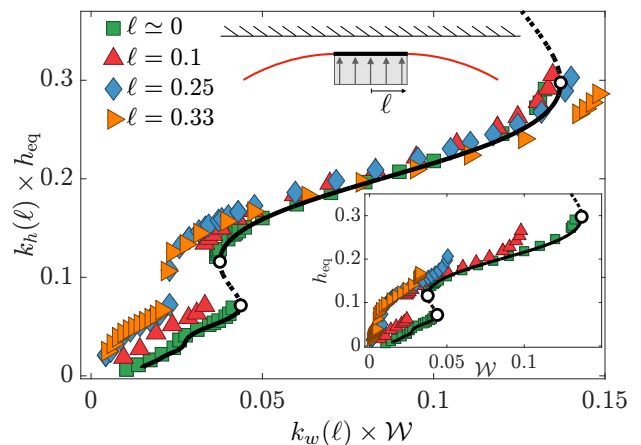


FIG. A2. Equilibrium averaged heights obtained by solving numerically (1) and (2) for $\alpha = 1.16$ and considering a rigid sheet for $|x| < \ell$. The label $\ell \simeq 0$ corresponds to a uniformly soft sheet with $\ell = 0.05$. The results collapse well when rescaling the height and weight to account for the rigid center. The inset shows the data without rescaling. Solid lines are the numerical continuation results from solving (5).

Appendix B: Finite motor size – When an actual motor generates the active forcing, as in the experimental setup of [12], it also locally rigidifies the sheet over its area of radius ℓ . We study this effect and solve numerically (1) and (2) for a sheet rigidified at its center; we obtain the equilibrium curves shown in Fig. A2. The important effect of a finite-size forcing and locally rigid sheet can be understood using scalings. From the analysis leading to (4), it is expected that incorporating the finite size effects ($\ell > 0$) leads to considering $\alpha^2 m(\ell)$ in place of α^2 . Also, a sheet with a rigid domain for $|\tilde{x}| < \tilde{\ell}$ is effectively stiffer compared to a soft one, with an effective bending modulus $\tilde{B}/(1 - \ell)^4$. From these considerations we expect that replacing h_{eq} with $h_{\text{eq}}/k_h(\ell)$ and \mathcal{W} with $\mathcal{W}/k_w(\ell)$ collapse the data, with correction factors $k_h(\ell) = (1 - \ell)^{4/3}$ and $k_w(\ell) = (m(\ell)/m(0))^2 (1 - \ell)^{8/3}$.

Figure A2 shows that this is indeed the case. The spread around the second equilibrium curve is expected as the rigid center more strongly affects higher-order modes. Therefore, for $\ell > 0$ (6) becomes

$$\begin{aligned} \tilde{W}_{\max} &= 0.11 \left(\frac{m(\ell)}{m(0)} \right)^2 (1 - \ell)^{8/3} \frac{(\tilde{m}\tilde{r}\tilde{\omega}^2)^2}{(\tilde{\mu}\tilde{\omega}\tilde{B}^2)^{1/3}}, \\ \tilde{h}_{\text{eq}}(\tilde{W}_{\max}) &= 0.19 (1 - \ell)^{4/3} \left(\frac{\tilde{\mu}\tilde{\omega}}{\tilde{B}} \right)^{1/3} \tilde{L}^2. \end{aligned} \quad (9)$$

Hovering of an actively driven fluid-lubricated foil – Supplementary Material

Stéphane Poulain, Timo Koch, and Andreas Carlson
Department of Mathematics, University of Oslo, 0851 Oslo, Norway

L. Mahadevan
*School of Engineering and Applied Sciences, Harvard University, Cambridge, Massachusetts 02138, USA and
 Departments of Physics, and of Organismic and Evolutionary Biology,
 Harvard University, Cambridge, Massachusetts 02138, USA*

I. BOUNDARY CONDITIONS

We consider an elastic sheet with free ends so that its edges have no bending moment, no twisting moment, and no shear force. These three boundary conditions cannot be imposed simultaneously using the Kirchhoff-Love hypotheses. Instead, it is appropriate to use the following (see [1, p. 586] and references therein for a discussion):

$$\mathbf{M}\mathbf{e}_r \cdot \mathbf{e}_r = 0, \quad (\nabla_{\perp} \cdot \mathbf{M}) \cdot \mathbf{e}_r + \nabla_{\perp} (\mathbf{M}\mathbf{e}_r \cdot \mathbf{e}_\theta) \cdot \mathbf{e}_\theta = 0, \quad (\text{S.1})$$

where \mathbf{e}_r is the outward unit normal at the edge of the sheet and \mathbf{e}_θ is the tangent. In 1D and in 2D axisymmetric cylindrical coordinates (with $r = |\mathbf{x}_{\perp}|$), this simplifies to:

$$\text{1D: at } x = \pm 1 : \quad \frac{\partial^2 h}{\partial x^2} = 0, \quad \frac{\partial}{\partial x} \left(\mathcal{B} \frac{\partial^2 h}{\partial x^2} \right) = 0, \quad (\text{S.2a})$$

$$\text{2D axisymmetric with } \mathcal{B} = \text{cst} : \quad \text{at } r = 1 : \quad \frac{\partial^2 h}{\partial r^2} + \frac{\nu}{r} \frac{\partial h}{\partial r} = 0, \quad \frac{\partial}{\partial r} (\nabla_{\perp}^2 h) = 0, \quad (\text{S.2b})$$

with $\nabla_{\perp}^2(\cdot) = \frac{1}{r} \frac{\partial}{\partial r} \left(r \frac{\partial}{\partial r}(\cdot) \right)$ the harmonic operator in cylindrical coordinates. In addition, the pressure at the edges recovers the atmospheric pressure so that:

$$\text{at } x = \pm 1 \text{ or } r = 1: \quad p = 0. \quad (\text{S.2c})$$

II. NUMERICAL METHOD

We numerically solve (1) and (2) in 1D, written in the form

$$\frac{\partial}{\partial t} (\mathbf{S}(\mathbf{U})) + \frac{\partial}{\partial x} (\mathbf{F}(\mathbf{U})) = \mathbf{Q}(\mathbf{U}), \quad (\text{S.3a})$$

with

$$\mathbf{S} = [h, 0, 0, 0], \quad \mathbf{F} = \left[0, -\frac{\partial m}{\partial x}, -\frac{\partial h}{\partial x}, p \right], \quad \mathbf{Q} = \left[v, p + f_n(x, t), \frac{m}{\mathcal{B}}, -\frac{12u}{h^2} \right], \quad (\text{S.3b})$$

and the primary unknowns $\mathbf{U} = [v = \partial h / \partial t, m = \mathcal{B} \partial^2 h / \partial x^2, h, u = q/h, p]$ representing the vertical sheet velocity, bending moment, height, averaged horizontal fluid velocity, and fluid pressure, respectively. The normal load $f_n(x, t) = f_a(x, t) + \mathcal{G}$ includes the active harmonic forcing and gravity. We solve for $x \in [-1, 1]$ with boundary conditions

$$m = 0, \quad \frac{\partial m}{\partial x} = 0, \quad p = 0. \quad (\text{S.3c})$$

The initial height is constant and systematically varied, while other variables are initially set to zero. The implementation is realized in the DuMu^x library [2]. We discretize in space using a staggered finite volume scheme with pressure unknown at cell centers and other unknowns at vertices; this avoids checkerboard oscillations. The state variables are advanced in time using a diagonally-implicit Runge-Kutta scheme of order 3 [3, Thm. 5], and the nonlinear system at each stage is solved with Newton's method. Lower-order time integration methods either yielded unsatisfactory accuracy or required excessively small timestep sizes. We used $\Delta t = 0.2$ and $0.015 \leq \Delta x \leq 0.05$ depending on the sheet's softness. For the results of Fig. 3, simulations ran until the averaged height reached an equilibrium, which could take $t = \mathcal{O}(10^4)$ up to $t = \mathcal{O}(10^6)$ depending on the dimensionless parameters.

III. FIRST-ORDER EFFECT OF THE SHEET'S ELASTICITY IN 1D

We consider a 1D uniform soft sheet and neglect gravity: $\mathcal{G} = 0$, $\gamma > 0$. The governing equations (1) and (2) read:

$$12 \frac{\partial h}{\partial t} - \frac{\partial}{\partial x} \left(h^3 \frac{\partial p}{\partial x} \right) = 0, \quad (\text{S.4a})$$

$$p = \mathcal{B} \frac{\partial^4 h}{\partial x^4} + \Gamma \phi_\ell(x) \cos(t), \quad (\text{S.4b})$$

with $\phi_\ell(x) = 1 - \mathbb{H}(|x| - \ell)$ and \mathbb{H} the Heaviside function. The boundary conditions at $x = \pm 1$ are given by (S.2):

$$\frac{\partial^2 h}{\partial x^2} = \frac{\partial^3 h}{\partial x^3} = p = 0. \quad (\text{S.4c})$$

We use a two-time scale expansion, $t \rightarrow (t, \tau)$, with t the time associated with the forcing and $\tau = \gamma t$ a slow time. We expand h as

$$h(x, t) = h_0(x, t, \tau) + \gamma h_1(x, t, \tau) + \gamma^2 h_2(x, t, \tau) + \mathcal{O}(\gamma^3). \quad (\text{S.5})$$

Inserting (S.5) into (S.4), we find at different order in γ :

$$\mathcal{O}(\gamma^{-1}) : \frac{\partial}{\partial x} \left(h_0^3 \frac{\partial^5 h_0}{\partial x^5} \right) = 0, \quad (\text{S.6a})$$

$$\mathcal{O}(1) : 12 \frac{\partial h_0}{\partial t} - \Gamma \ell h_0^3 \frac{\partial^6 h_1}{\partial x^6} - \Gamma \cos(t) h_0^3 \frac{\partial^2 \phi_\ell}{\partial x^2} = 0, \quad (\text{S.6b})$$

$$\mathcal{O}(\gamma) : 12 \frac{\partial h_1}{\partial t} + 12 \frac{\partial h_0}{\partial \tau} - \Gamma \ell h_0^3 \frac{\partial^6 h_2}{\partial x^6} - 3 \Gamma \ell h_0^2 \frac{\partial}{\partial x} \left(h_1 \frac{\partial^5 h_1}{\partial x^5} \right) - 3 \Gamma h_0^2 \cos(t) \frac{\partial}{\partial x} \left(h_1 \frac{\partial \phi_\ell}{\partial x} \right) = 0. \quad (\text{S.6c})$$

We note that (S.6a) gives $h_0 = h_0(t, \tau)$, and we have used this to simplify (S.6b) and (S.6c) already. The associated boundary conditions, (S.4c), at $x = \pm 1$ become:

$$\mathcal{O}(1) : \frac{\partial^2 h_1}{\partial x^2} = \frac{\partial^3 h_1}{\partial x^3} = 0, \quad \frac{\partial^4 h_1}{\partial x^4} = -\frac{\phi_\ell(1)}{\ell} \cos(t), \quad (\text{S.7a})$$

$$\mathcal{O}(\gamma) : \frac{\partial^2 h_2}{\partial x^2} = \frac{\partial^3 h_2}{\partial x^3} = \frac{\partial^4 h_2}{\partial x^4} = 0. \quad (\text{S.7b})$$

A. Calculations to $\mathcal{O}(1)$

We integrate (S.6b) in space six times, using the boundary conditions (S.7a) and the fact that the sheet is symmetric ($\partial h / \partial x = \partial^3 h / \partial x^3 = \partial^5 h / \partial x^5 = 0$ at $x = 0$) to express h_1 as:

$$h_1(x, t) = b(t, \tau) + \cos(t) H_{1,\ell}(x), \quad (\text{S.8a})$$

where $b(t, \tau)$ is an integration constant to be determined. The function $H_{1,\ell}(x)$ is polynomial by part, given by

$$H_{1,\ell}(x) = \frac{1}{24} \left(-\frac{3(4\ell - 3)x^2}{2} + \frac{(3\ell - 2)x^4}{2\ell} - \frac{x^6}{10} + \frac{(x - \ell)^4}{\ell} \mathbb{H}(x - \ell) \right) \quad \text{for } x > 0. \quad (\text{S.8b})$$

For $x < 0$, the expression is due the parity of $H_{1,\ell}$. Because the following particular cases of the function $H_{1,\ell}(x)$ will be used later, we write explicitly $H_{1,0}(x)$ corresponding to a point load $\ell = 0$, and $H_{1,1}(x)$ corresponding to a uniform load $\ell = 1$:

$$\begin{aligned} H_{1,0}(x) &= -\frac{x^6}{240} + \frac{x^4}{16} - \frac{x^3}{6} + \frac{3x^2}{16} \quad \text{for } x > 0, \\ H_{1,1}(x) &= -\frac{x^6}{240} + \frac{x^4}{48} - \frac{x^2}{16} \quad \forall x. \end{aligned} \quad (\text{S.8c})$$

Integrating (S.6b) and applying the boundary conditions also gives an ordinary differential equation (ODE) for h_0 that admits the solution

$$h_0(t, \tau) = \left(f(\tau) + \frac{\Gamma \ell}{2} \sin t \right)^{-1/2}, \quad (\text{S.9})$$

with $f(\tau)$ an integration constant to be determined.

B. Calculations to $\mathcal{O}(\gamma)$

Using (S.8a) and (S.9), (S.6c) becomes:

$$\frac{\partial^6 h_2}{\partial x^6} = \left(\frac{12}{\Gamma \ell h_0^3(t, \tau)} \frac{\partial b}{\partial t} - \frac{6}{\Gamma \ell} f'(\tau) + \frac{9b(t, \tau) \cos(t)}{h_0} \right) + \left(-\frac{12 \sin(t)}{\Gamma \ell h_0^3(t, \tau)} H_{1, \ell}(x) + \frac{9 \cos^2(t)}{h_0(t, \tau)} \frac{\partial}{\partial x} (x H_{1, \ell}(x)) \right). \quad (\text{S.10})$$

We again integrate in space six times, using the boundary conditions (S.7b) and symmetry at $x = 0$. This yields an expression for h_2 and an ODE for the function b in time t :

$$h_2(x, t, \tau) = \beta(t, \tau) + \frac{\sin(t)}{\Gamma \ell h_0^3(t, \tau)} 12 H_{2, \ell}(x) + \frac{\cos^2(t)}{h_0(t, \tau)} 9 H_{2, \ell}^*(x), \quad (\text{S.11})$$

$$\frac{\partial b}{\partial t} + \frac{3}{4} \frac{\Gamma \ell \cos(t)}{f(\tau) + \frac{\Gamma \ell}{2} \sin(t)} b(t, \tau) = 720 P_6(\ell) \sin(t) + 630 Q_6(\ell) \frac{\Gamma \ell \cos^2(t)}{f(\tau) + \frac{\Gamma \ell}{2} \sin(t)} + \frac{f'(\tau)}{2 (f(\tau) + \frac{\Gamma \ell}{2} \sin(t))^{3/2}}. \quad (\text{S.12})$$

The function $\beta(t, \tau)$ is an integration constant, and the functions $H_{2, \ell}(x)$, $H_{2, \ell}^*(x)$ are piecewise polynomials of order 12 whose coefficients depend on ℓ ; P_6 and Q_6 are 7th-order polynomials. They are given by:

$$\begin{aligned} H_{2, \ell}(x) &= P_2(\ell) x^2 + P_4(\ell) x^4 + P_6(\ell) x^6 + \mathcal{H}_{2, \ell}(x), \\ H_{2, \ell}^*(x) &= Q_2(\ell) x^2 + Q_4(\ell) x^4 + Q_6(\ell) x^6 + \mathcal{H}_{2, \ell}^*(x), \\ \mathcal{H}_{2, \ell}(x) &= \frac{1}{10!} \left[\frac{45(4\ell - 3)x^8}{4} + \frac{(3\ell - 2)x^{10}}{2\ell} + \frac{x^{12}}{44} + \frac{(x - \ell)^{10}}{\ell} \mathbb{H}(x - \ell) \right], \\ \mathcal{H}_{2, \ell}^*(x) &= \frac{1}{10!} \left[-\frac{135(4\ell - 3)x^8}{4} + \frac{5(3\ell - 2)x^{10}}{2\ell} - \frac{7x^{12}}{44} + 5 \frac{(x - \ell)^9(x + \ell)}{\ell} \mathbb{H}(x - \ell) \right], \\ P_2(\ell) &= \frac{1}{20 \times 8!} (103 - 210\ell^2 + 70\ell^4 - 30\ell^6 + 10\ell^7), \quad Q_2(\ell) = \frac{-1}{20 \times 8!} (241 - 420\ell^2 + 60\ell^6 - 30\ell^7), \\ P_4(\ell) &= \frac{-1}{24 \times 8!} (65 - 140\ell^2 + 84\ell^4 - 56\ell^5 + 12\ell^6), \quad Q_4(\ell) = \frac{1}{24 \times 8!} (155 - 280\ell^2 + 56\ell^5 - 24\ell^6), \\ P_6(\ell) &= \frac{1}{10!} (110 - 315\ell^2 + 210\ell^3 - 63\ell^4 + 3\ell^6), \quad Q_6(\ell) = \frac{1}{10!} (-275 + 630\ell^2 - 210\ell^3 + 6\ell^6). \end{aligned} \quad (\text{S.13})$$

These expressions are valid for $x > 0$; for negative x , one can use the parity of the height profile.

Equation (S.12) is a first-order linear ODE in t for b that has the solution

$$\begin{aligned} b(t, \tau) &= 90 \left(1 + \frac{\Gamma \ell}{2} \sin(t) \right)^{-3/2} \left[\frac{t}{2} \frac{df}{d\tau} + 8P_6(\ell) \int_0^t \sin(t') \left(f(\tau) + \frac{\Gamma \ell}{2} \sin(t') \right)^{3/2} dt' + \right. \\ &\quad \left. + 7Q_6(\ell) \Gamma \ell \int_0^t \cos^2(t') \left(f(\tau) + \frac{\Gamma \ell}{2} \sin(t') \right)^{1/2} dt' \right]. \end{aligned} \quad (\text{S.14})$$

We choose $f(\tau)$ to ensure that there are no secular terms such that the asymptotic expansion (S.5) remains valid: this is achieved by requesting b to be 2π -periodic in t (otherwise b would be unbounded). The condition $b(2\pi) = b(0)$, with $b(0) = 0$, gives an ODE in τ for f . We approximate the integrals appearing in (S.14) using a first-order Taylor expansion for small $\Gamma \ell / 2f(\tau)$ to find:

$$\begin{aligned} f'(\tau) &= \Gamma \ell m(\ell) f(\tau)^{1/2}, \quad f(\tau) = \left(1 - \frac{m(\ell)}{2} \Gamma \ell \tau \right)^2, \\ h_0(t) &= \left[\left(1 + \frac{m(\ell)}{2} \frac{(\Gamma \ell)^2}{B} t \right)^2 + \frac{\Gamma \ell}{2} \sin(t) \right]^{-1/2}, \quad m(\ell) = -90 (6P_6(\ell) + 7Q_6(\ell)). \end{aligned} \quad (\text{S.15})$$

IV. STABLE HOVERING HEIGHT IN 1D: EQUILIBRIA FOR SOFT SHEETS WITH WEIGHT

Here we consider (S.4) using the heightscale $\tilde{H}_{bv} = \tilde{L}^2 (\tilde{\mu}\tilde{\omega}/\tilde{B})$, i.e., we let $\tilde{H} \equiv \tilde{H}_{bv}$ in all dimensionless expressions involving \tilde{H} . We also consider $\ell \rightarrow 0$. With these considerations, we can write (S.4) as:

$$12 \frac{\partial h}{\partial t} - \frac{\partial}{\partial x} \left(h^3 \frac{\partial p}{\partial x} \right) = 0, \quad (\text{S.16a})$$

$$p = \frac{\partial^4 h}{\partial x^4} + \alpha \phi_0(x) \cos(t), \quad (\text{S.16b})$$

$$\text{at } x = \pm 1 : \quad \frac{\partial^2 h}{\partial x^2} = \frac{\partial^3 h}{\partial x^3} = p = 0. \quad (\text{S.16c})$$

Equations (S.16a) and (S.16b) without load ($\alpha = 0$) simplify to $\partial h/\partial t - \partial/\partial x (h^3 \partial^5 h/\partial x^5) = 0$. Linearizing with $h = 1 + u$, $|u| \ll 1$ gives $\partial u/\partial t - \partial^6 u/\partial x^6 = 0$. This motivates to project (S.16) in space using the eigenfunctions of the tri-harmonic operator subject to appropriate boundary conditions:

$$\begin{aligned} \frac{\partial^6 \zeta}{\partial x^6} + k^6 \zeta &= 0 \quad \text{for } -1 \leq x \leq 1, \\ \frac{\partial^2 \zeta}{\partial x^2} = \frac{\partial^3 \zeta}{\partial x^3} = \frac{\partial^4 \zeta}{\partial x^4} &= 0 \quad \text{at } x = \pm 1. \end{aligned} \quad (\text{S.17})$$

We only seek the even modes. The nontrivial solutions ζ_n to (S.17) are found by solving an eigenvalue problem. They only exist for discrete values k_n of k . For n a positive integer, we find that the associated eigenfunctions ζ_n are given by:

$$\begin{aligned} k_n &= n\pi, \\ \zeta_n(x) &= I_n \left[A_n \cos(k_n x) + B_n \cosh \left(k_n \frac{\sqrt{3}}{2} x \right) \cos \left(\frac{k_n}{2} x \right) + C_n \sinh \left(k_n \frac{\sqrt{3}}{2} x \right) \sin \left(\frac{k_n}{2} x \right) \right], \\ \text{if } n \text{ even, } \begin{cases} A_n &= \frac{1}{2}(-1)^{n/2} \cosh \left(\frac{\sqrt{3}}{2} k_n \right) \\ B_n &= 1 \\ C_n &= 0 \end{cases} ; \quad \text{else, } \begin{cases} A_n &= -\frac{1}{2}(-1)^{(n-1)/2} \sinh \left(\frac{\sqrt{3}}{2} k_n \right) \\ B_n &= 0 \\ C_n &= 1 \end{cases}, \end{aligned} \quad (\text{S.18})$$

with I_n a coefficient ensuring $\int_{-1}^1 \zeta_n^2(x) dx = 1$. We then seek the solution of (S.16) using the following ansatz, with $H_{1,0}$ and $H_{1,1}$ defined earlier in (S.8c):

$$p(x, t) = \frac{3}{2} (\mathcal{W}\alpha^2 + \alpha \cos(t)) (1 - x^2) + \alpha \sum_{i=1}^N a_i(t) \zeta_i^{(4)}(x), \quad (\text{S.19a})$$

$$h(x, t) = h_0(t) + \alpha^2 \mathcal{W} H_{1,1}(x) + \alpha \cos(t) H_{1,0}(x) + \alpha \sum_{i=1}^N a_i(t) \zeta_i(x).$$

These expressions ensure that the normal force balance (S.16b) as well as the boundary conditions (S.16c) are satisfied, and they recover the analysis of §III at $\mathcal{O}(\alpha)$. The height $h_0(t)$ and the N coefficients $a_i(t)$ are found by projecting (S.16a) on the ζ_i , giving a coupled set of $N + 1$ ODEs in t :

$$\text{for } 0 \leq i \leq N : \quad \int_0^1 \left[12 \frac{\partial h}{\partial t} - \frac{\partial}{\partial x} \left(h^3 \frac{\partial p}{\partial x} \right) \right] \zeta_i(x) dx = 0, \quad (\text{S.19b})$$

where we let $\zeta_0(x) = \sqrt{2}/2$.

A. Projection onto a single mode

We first focus on describing the dynamics using the first mode $\zeta_1(x)$ only, i.e., $N = 1$. Previous calculations from §III show that the system is more naturally studied after a change of variable: we introduce $F(t)$ as

$$h_0(t) = \left[F(t) + \frac{\alpha}{2} \sin(t) \right]^{-1/2}. \quad (\text{S.20})$$

After computing the integrals resulting from (S.19b) (we perform the averaging in space numerically using Wolfram Mathematica) and expanding in powers of α , we obtain differential equations for $F(t)$ and $a_1(t)$. In particular,

$$\frac{dF}{dt} = \alpha c_0 F^{3/2}(t) \sin(t) + \mathcal{O}(\alpha^2), \quad \text{with } c_0 \simeq 0.04356 \quad (\text{S.21})$$

a coefficient found numerically. This motivates another change of variable: we introduce $\eta(t)$ as

$$\eta(t) = F^{-1/2}(t) - \alpha \frac{c_0}{2} \cos(t) = \left(h_0^{-2}(t) - \frac{\alpha}{2} \sin(t) \right)^{-1/2} - c_0 \frac{\alpha}{2} \cos(t). \quad (\text{S.22})$$

We note that $\eta(t) = h_0(t) + \mathcal{O}(\alpha)$, and, therefore, $\eta(t)$ directly describes the height evolution.

Using $\eta(t)$ and $a_1(t)$ as the two independent variables, we arrive at the following differential system:

$$\frac{d\eta}{dt} = \alpha^2 \eta^2 \left[-\frac{1}{4} \mathcal{W}\eta(t) + c_1 + c_2 \cos(2t) + c_3 \cos(t) a_1(t) + c_4 a_1(t)^2 \right] + \mathcal{O}(\alpha^3), \quad (\text{S.23a})$$

$$\frac{da_1}{dt} = c_5 \sin(t) + c_6 \eta^3(t) a_1(t) + \mathcal{O}(\alpha), \quad (\text{S.23b})$$

with the c_i constant coefficients found numerically. Equation (S.23a) shows that $d\eta/dt = \mathcal{O}(\alpha^2)$. We follow ideas from the averaging method [4, 5]. We introduce a slow time $T = \alpha^2 t$, consider $\eta = \eta(T)$ and $a_1 = a_1(t, T)$, and apply the averaging operator $\langle u \rangle = \int_t^{t+2\pi} u(t') dt' / 2\pi$ to (S.23a). We find:

$$\frac{d\eta}{dT} = \eta^2(T) \left[-\frac{1}{4} \mathcal{W}\eta(T) + c_1 + c_3 \langle \cos(t) a_1(t, T) \rangle + c_4 \langle a_1(t, T)^2 \rangle \right] + \mathcal{O}(\alpha^3). \quad (\text{S.24})$$

To describe the height dynamics at $\mathcal{O}(\alpha^2)$, it suffices to express $a_1(t, T)$ at $\mathcal{O}(1)$. At this order, (S.23b) is a linear ODE in t (since $\eta(t)$ becomes $\eta(T)$) that is solved as

$$a_1(t, T) = -c_5 \frac{\cos(t)}{1 + c_6^2 \eta^6(T)} - c_5 c_6 \frac{\eta^3(T) \sin(t)}{1 + c_6^2 \eta^6(T)}. \quad (\text{S.25})$$

Another term proportional to $\exp[c_6 t \eta^3(T)]$ appears in the general solution for a_1 ; we cancel it by setting the associated integration constant to zero. This amounts to considering the appropriate initial condition for a_1 that prevents an initial fast transient dynamic, i.e., $a_1(t=0) = -c_5 / (1 + c_6^2 \eta^6(0))$.

Inserting (S.25) into (S.24) finally gives an autonomous differential equation that describes the dynamics of the averaged height evolution dynamic at $\mathcal{O}(\alpha^2)$:

$$\frac{d\eta}{dT} = \eta^2 \left[\frac{1}{4} \mathcal{W}\eta - d_0 + \frac{d_1}{1 + \left(\frac{\eta}{e_1} \right)^6} \right], \quad T = \alpha^2 t, \quad (\text{S.26})$$

$$d_0 = 0.0122, \quad d_1 = 0.0113, \quad e_1 = 0.232,$$

with d_0 , d_1 and e_1 constants found from the spatial projection.

B. Projection onto several modes

The procedure described in the previous section can be applied similarly with $N > 1$ modes. We find that the system of $N + 1$ differential equations obtained from (S.19b) can be rewritten as:

$$\frac{d\eta}{dt} = \mathcal{O}(\alpha^2),$$

$$\text{for } 1 \leq i \leq N : \quad \frac{da_i}{dt} = k_{1,i} \sin(t) + k_{2,i} \eta^3(t) a_i(t) + \mathcal{O}(\alpha),$$

with the $k_{1,i}$ and $k_{2,i}$ numerical coefficients. This allows us to use the same averaging procedure: we solve explicitly for the a_i at $\mathcal{O}(1)$, which gives us the averaged dynamics of η at $\mathcal{O}(\alpha^2)$. After calculations analogous to the ones shown in the previous paragraph, the solution takes the form

$$\frac{d\eta}{dT} = \eta^2 \left[\frac{1}{4} \mathcal{W}\eta - d_0 + \sum_{i=1}^N \frac{d_{ii}}{1 + \left(\frac{\eta}{e_i}\right)^6} + \sum_{i=1}^N \sum_{j=i+1}^N \frac{d_{ij} \left(1 + \left(\frac{\eta}{\sqrt{e_i e_j}}\right)^6\right)}{\left(1 + \left(\frac{\eta}{e_i}\right)^6\right) \left(1 + \left(\frac{\eta}{e_j}\right)^6\right)} \right], \quad T = \alpha^2 t. \quad (\text{S.27})$$

Up to $N = 5$, we find $d_0 = 1.22 \times 10^{-2}$ and

$$\mathbf{e} = \begin{pmatrix} 0.23 \\ 0.058 \\ 0.026 \\ 0.015 \\ 0.0093 \end{pmatrix}, \quad \mathbf{d} = \begin{pmatrix} 1.14 \times 10^{-2} & 2.04 \times 10^{-6} & -6.91 \times 10^{-6} & 1.64 \times 10^{-5} & -3.24 \times 10^{-5} \\ & 6.95 \times 10^{-4} & 9.24 \times 10^{-7} & -2.05 \times 10^{-6} & 4.01 \times 10^{-6} \\ & & 1.49 \times 10^{-4} & 7.08 \times 10^{-7} & -1.24 \times 10^{-6} \\ & & & 3.00 \times 10^{-5} & 6.12 \times 10^{-7} \\ & & & & 4.73 \times 10^{-5} \end{pmatrix}, \quad (\text{S.28})$$

where \mathbf{e} is the vector with coefficient e_i and \mathbf{d} the symmetrical matrix with coefficients d_{ij} .

V. AXISYMMETRIC CIRCULAR SHEETS

Here, we adapt the analysis of a 1D soft sheet to study a 2D circular and axisymmetric sheet. The methods and reasoning are identical to those in the 1D case. We present only the final results below, using the same notations as in §III for the first part when we consider weightless sheets, and of §IV for the second part considering the weight of the sheet. We only note that $\Gamma\ell$ becomes $\Gamma\ell^2$ when transposing 1D to 2D, since the normal force balance is considered per unit length in the 1D case and per unit area in the 2D case.

A. Soft weightless sheets

Here, we consider $\mathcal{G} = 0$ and keep the heightscale H arbitrary. The spatial variable is now $r = |\mathbf{x}_\perp|$. The governing equations (1) and (2) read:

$$12 \frac{\partial h}{\partial t} - \frac{1}{r} \frac{\partial}{\partial r} \left(r h^3 \frac{\partial p}{\partial r} \right) = 0, \quad (\text{S.29a})$$

$$p = \mathcal{B} \nabla_\perp^4 h + \Gamma \phi_\ell(r) \cos(t), \quad (\text{S.29b})$$

with boundary conditions at $r = 1$ from (S.2):

$$p = 0, \quad \frac{\partial^2 h}{\partial r^2} + \frac{\nu}{r} \frac{\partial h}{\partial r} = 0, \quad \frac{\partial}{\partial r} (\nabla_\perp^2 h) = 0. \quad (\text{S.29c})$$

With $h(x, t) = h_0(x, t, \tau) + \gamma h_1(x, t, \tau)$, $\tau = \gamma t$, we find:

$$h_0(t) = \left(f(\tau) + \frac{4\Gamma\ell^2}{3} \sin(t) \right)^{-1/2}, \quad (\text{S.30a})$$

$$h_1 = \alpha(t, \tau) + \cos(t) H_{1,\ell}(r),$$

with

$$H_{1,\ell}(r) = \frac{1}{4} \left(\phi_\nu(\ell) r^2 + \frac{2\ell^2 - 1}{16\ell^2} r^4 - \frac{r^6}{72} + \frac{\mathbb{H}(r - \ell)}{16} \left[\frac{r^4}{\ell^2} + 4r^2 - 5\ell^2 - 4(\ell^2 + 2r^2) \ln\left(\frac{r}{\ell}\right) \right] \right), \quad (\text{S.30b})$$

$$\phi_\nu(\ell) = -\frac{(1 + 5\nu) + 3(1 - \nu)\ell^2}{24(1 + \nu)} - \frac{1}{2} \ln(\ell),$$

and

$$f(\tau) = \left(1 - \frac{m(\ell)}{2}\Gamma\ell\tau\right)^2, \quad (\text{S.30c})$$

$$m(\ell) = \frac{67 + 27\nu}{2888(1 + \nu)} - \frac{2 + \nu}{48(1 + \nu)}\ell^2 + \frac{\ell^4}{96} - \frac{\ell^6}{576}.$$

The coefficient $m(\ell)$ and the $\mathcal{O}(\gamma)$ deformation mode $H_{1,\ell}(r)$ are shown in Fig. S.1. We notice the same correlation discussed in the main text for the 1D case between the sign of $m(\ell)$ and the convexity of $H_{1,\ell}(r)$. We also note that the Poisson's ratio ν now appears explicitly in these expressions because of the boundary conditions (S.29c). We will specifically need in the next section the deformation for $\ell = 0$ and $\ell = 1$:

$$H_{1,1}(r) = -\frac{r^6}{288} + \frac{r^4}{64} - \frac{2 + \nu}{48(1 + \nu)}r^2, \quad (\text{S.30d})$$

$$H_{1,0}(r) = -\frac{r^6}{288} + \frac{r^4}{32} + \frac{5 + \nu}{96(1 + \nu)}r^2 - \frac{1}{8}r^2 \ln(r).$$

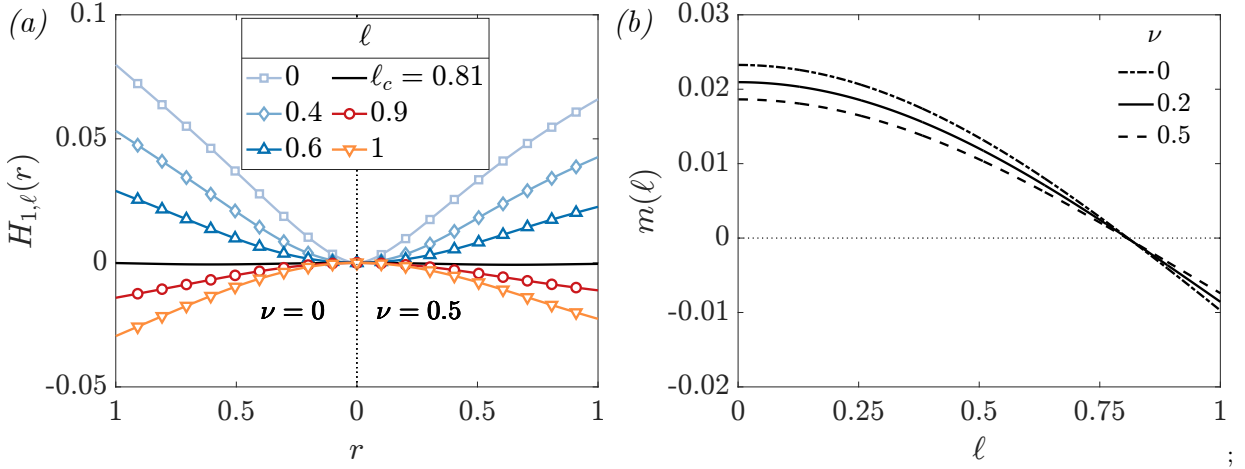


FIG. S.1: Characterization of the dynamics of a circular soft weightless sheet from (S.30).

B. Soft sheets with weight

Here, we consider $\mathcal{G} > 0$. We follow the same steps as in §IV, letting $\tilde{H} = \tilde{H}_{bv}$, $\alpha = \Gamma\ell^2|_{\tilde{H}=\tilde{H}_{bv}}$ and $\mathcal{W} = \mathcal{G}/\alpha^2$. Moreover, $\ell \rightarrow 0$. We project the height $h(r, t)$ on the eigenfunctions of the tri-harmonic operator in axisymmetric cylindrical coordinates. Factorizing $(\nabla_{\perp}^6 + k^6)\zeta = (\nabla_{\perp}^2 + k^2)(\nabla_{\perp}^2 - k^2j)(\nabla_{\perp}^2 + k^2j^2)\zeta$, we find that the solutions of $(\nabla_{\perp}^6 + k^6)\zeta = 0$ have the form:

$$\zeta_n(r) = A_n J_0(k_n r) + B_n J_0(jk_n r) + C_n J_0(j^2 k_n r), \quad (\text{S.31})$$

with J_m the Bessel function of the first kind of m -th order and $j = e^{-2i\pi/3}$; the cube roots of 1 are 1, j , j^2 . The boundary conditions (S.29c) (we use $\nabla_{\perp}^4 g_n = 0$ in lieu of $p = 0$) give the following constraints:

$$\begin{pmatrix} J_0(k_n) & -jJ_0(jk_n) & j^2 J_0(j^2 k_n) \\ J_1(k_n) & -J_1(jk_n) & J_1(j^2 k_n) \\ -kJ_0(k_n) + (1 - \nu)J_1(k_n) & j^2 k J_0(jk_n) - j(1 - \nu)J_1(jk_n) & jk J_0(j^2 k_n) + j^2(1 - \nu)J_1(j^2 k_n) \end{pmatrix} \begin{pmatrix} A_n \\ B_n \\ C_n \end{pmatrix} = 0. \quad (\text{S.32})$$

The family of k_n 's and associated eigenvectors that allow for nontrivial solutions give the corresponding coefficients A_n, B_n, C_n . For a given choice of ν , (S.32) can be solved numerically. For $\nu = 0.3$ and 0.5, we find that the first

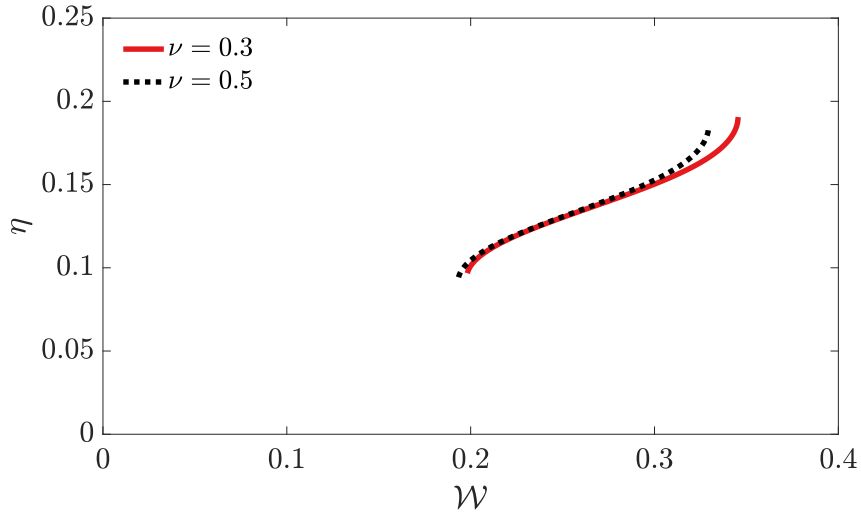


FIG. S.2: Stable equilibrium of an axisymmetric obtained from (4) with $N = 1$ and coefficients given by (S.36).

eigenmodes are given by:

$$\begin{aligned}
 \nu = 0.3 : & \begin{cases} k_1 = 3.8456, & A_1 = 1, & B_1 = 0.0118 - 0.0793i, & C_1 = \bar{B}_1, \\ k_2 = 7.0022, & A_2 = 1, & B_2 = -4.92 \times 10^{-3} - 6.68 \times 10^{-4}i, & C_2 = \bar{B}_2, \\ k_3 = 10.1605, & A_3 = 1, & B_3 = -4.18 \times 10^{-5} + 3.13 \times 10^{-4}i, & C_3 = \bar{B}_3, \end{cases} \\
 \nu = 0.5 : & \begin{cases} k_1 = 3.8933, & A_1 = 1, & B_1 = 0.0107 - 0.0725i, & C_1 = \bar{B}_1, \\ k_2 = 7.0311, & A_2 = 1, & B_2 = -4.68 \times 10^{-3} - 6.35 \times 10^{-4}i, & C_2 = \bar{B}_2, \\ k_3 = 10.1805, & A_3 = 1, & B_3 = -4.04 \times 10^{-5} + 3.03 \times 10^{-4}i, & C_3 = \bar{B}_3. \end{cases}
 \end{aligned} \tag{S.33}$$

The bar denotes the complex conjugate. We note that the associated eigenfunctions are real-valued.

The ansatz we use for the pressure and height that satisfies the boundary conditions and the normal force balance is then:

$$\begin{aligned}
 p(r, t) &= 2(\mathcal{W}\alpha^2 + \alpha \cos(t))(1 - r^2) + \alpha \sum_{i=1}^N a_i(t) \nabla_{\perp}^4 g_i(x), \\
 h(r, t) &= h_0(t) + \mathcal{W}\alpha^2 H_{1,1}(r) + \alpha \cos(t) H_{1,0}(r) + \alpha \sum_{i=1}^N a_i(t) g_i(r).
 \end{aligned} \tag{S.34}$$

The coefficients h_0 and a_i are determined by the $(N + 1)$ equations:

$$\text{for } 0 \leq i \leq N : \quad \int_0^1 \left[12 \frac{\partial h}{\partial t} - \frac{1}{r} \frac{\partial}{\partial r} \left(r h^3 \frac{\partial p}{\partial r} \right) \right] g_i(r) r dr = 0, \tag{S.35}$$

where we let $\zeta_0(r) = 1$, resulting in a system of $n + 1$ ODEs.

We follow the same averaging and rescaling procedure to arrive at the analog of (S.27). For 2D sheets, the resulting ODE has the same structure and only differs by the numerical prefactors $(e_i)_{i=1 \dots N}$, d_0 and $(d_{ij})_{i,j=1 \dots N}$. At $N = 1$, which suffices to find the maximum supported weight \mathcal{W}_{\max} , we find:

$$\begin{aligned}
 \nu = 0.3 : & \quad e_1 = 0.155, \quad d_0 = 2.00 \times 10^{-2}, \quad d_{11} = 1.61 \times 10^{-2}, \\
 \nu = 0.5 : & \quad e_1 = 0.151, \quad d_0 = 1.86 \times 10^{-2}, \quad d_{11} = 1.47 \times 10^{-2}.
 \end{aligned} \tag{S.36}$$

VI. MOVIE DESCRIPTIONS

Movies S1 & S2: Schematic illustrations of the adhesion (Movie S1, $\ell < \ell_c$) and repulsion (Movie S2, $\ell > \ell_c$) mechanisms in the absence of gravity. The foil's displacement and deformation are computed from the analysis of

Section III and amplified for clarity. The pressure profile is computed from the force balance (2) and the velocity vectors are obtained from the height and pressure profiles following classical lubrication theory [6].

Movie S3: Numerical results ($\alpha = 2$, $\ell = 0.05$, $\mathcal{W} = 0.13$) in the absence of gravity illustrating how the foil fails to adhere when it is too heavy.

Movie S4: Numerical results ($\alpha = 2$, $\ell = 0.05$, $\mathcal{W} = 0.10$) showing the foil reaching the first equilibrium branch at $h_{\text{eq}} \simeq 0.10$. Once a time-averaged steady state is reached, we analyze the sheet’s deformations using a Principal Component Analysis (PCA) on $h'(x, t) = h(x, t) - \langle h \rangle(x) - \bar{h}(t) + \langle \bar{h} \rangle$, where $\langle h \rangle$ is the temporal average and \bar{h} the spatial average of the height profile. This is defined such that $\langle h' \rangle(x) = \bar{h}'(t) = 0$. We show the evolution of $h(x, t) - h'(x, t)$, the combination of the foil’s translation mode and of its static deformation due to gravity, and the first spatial modes captured by the PCA of h' . In short, the spatial profile of h' at each timestep is stored in a column of the matrix \mathbf{H}' . The singular value decomposition $\mathbf{H}' = \mathbf{U}\mathbf{\Sigma}\mathbf{V}^*$ allows to identify the dominant modes corresponding to the largest values of the diagonal matrix $\mathbf{\Sigma}$.

Movie S5: Numerical results ($\alpha = 2$, $\ell = 0.05$, $\mathcal{W} = 0.03$) showing the foil reaching the second equilibrium branch at $h_{\text{eq}} \simeq 0.05$. We perform the same analysis as for Movie S4.

-
- [1] P. M. Naghdi, “The theory of shells and plates,” in *Linear theories of elasticity and thermoelasticity: linear and nonlinear theories of rods, plates, and shells* (Springer, 1973) pp. 425–640.
 - [2] T. Koch, D. Gläser, K. Weishaupt, *et al.*, “DuMux 3 – an open-source simulator for solving flow and transport problems in porous media with a focus on model coupling,” *Computers & Mathematics with Applications* **81**, 423–443 (2021).
 - [3] Roger Alexander, “Diagonally implicit Runge-Kutta methods for stiff O.D.E.’s,” *SIAM Journal on Numerical Analysis* **14**, 1006–1021 (1977).
 - [4] J.A. Sanders, F. Verhulst, and J. Murdock, *Averaging methods in nonlinear dynamical systems*, Vol. 59 (Springer, 2007).
 - [5] F. Verhulst, *A Toolbox of Averaging Theorems: Ordinary and Partial Differential Equations*, Vol. 12 (Springer Nature, 2023).
 - [6] G.K. Batchelor, *An Introduction to Fluid Dynamics* (Cambridge University Press, 1967).